Article:

Lai, F., Cao, C., Shi, C. et al. (8 more authors) (2025) Improvement of wear resistance for engine valve: Introducing cold upsetting treatment on valve seating face. Wear, 564-565. 205693. ISSN 0043-1648

https://doi.org/10.1016/j.wear.2024.205693

Improvement of wear resistance for engine valve: introducing cold upsetting treatment on valve seating face

Fuqiang Lai[1], Changsheng Cao[1], Chuangwei Shi[1], Ge Sun[2], Rong Qu[2], Dongqiang Mo[2], Youxi Lin[1], Shengguan Qu[3], Roger Lewis[4], Tom Slatter[5], Xin Xue*[1]

1. School of Mechanical Engineering and Automation, Fuzhou University, Fuzhou 350116, Fujian, China

2. Huaiji Dengyue Valve Co., Ltd., Huaiji County526400, Guangdong, China

3. School of Mechanical and Automotive Engineering, South China University of Technology, Guangzhou 510640, Guangdong, China

4. Department of Mechanical Engineering, The University of Sheffield, Mappin Street, Sheffield, UK, S1 3JD

5. School of Mechanical, Electrical & Manufacturing Engineering, Loughborough University, Epinal Way, Loughborough, U.K. LE11 3TU

*Correspondence: xin@fzu.edu.cn

Abstract

This study presents a new surface strengthening technique (cold upsetting manufacturing process) for engine valve seating face (VSF). The properties of the Ni30 superalloy VSF were characterized before and after cold upsetting. Compared to the solution-aging treatment (SAT) valve, the solution-cold upsetting-aging treatment (SCUAT) valve hardness was increased by 60 $HV_{0.2}$. SCUAT valves exhibited higher internal dislocation degrees and local misorientation than SAT valves. Bench-top wear tests at 650 °C and 750 °C were conducted. The valve wear loss at 650 °C was higher than that at 750 °C. SCUAT valves show better wear resistance, with a total wear loss reduction up to 26.76%. The SCUAT valve-seat insert contact pair wear mechanisms are adhesive and fatigue wear.

Keywords: Internal combustion engine exhaust valve; Valve seating face; Plastic deformation processing; Wear mechanisms

Highlights

The solution-cold upsetting-aging treatment (SCUAT) was applied to engine valve.

SCUAT produced a significant increase in low-angle grain boundaries of valve.

SCUAT can significantly improve the hardness of the valve samples.

The wear resistance of valve seating face was increased after SCUAT.

The high-temperature wear mechanism is a combination of adhesive and fatigue wear.

List of abbreviations and symbols

SAT	Solution-aging treatment	SCUAT	Solution-cold upsetting-aging treatment
VSF	Valve seating face	VSI	Valve seat insert
ICE	Internal combustion engine	SEM	Scanning electron microscopy
EBSD	Electron back scatter diffraction	XRD	X-ray diffractometer
EDS	Energy–dispersive spectroscopy	GD	Grain diameter
LAGB	Low angle grain boundaries	HAGB	High angle grain boundaries

1. Introduction

There is an industrial demand for internal combustion engines (ICEs) to be developed to be smaller and more powerful, leading to an increase in combustion chamber temperature and pressure. Traditional solid exhaust valve head temperatures can reach up to 750 ºC [1, 2]. The schematic diagram of a valve working in an ICE is shown in Fig. 1, where the valve is subjected to repeated impact loads in high-temperature oxidizing and corrosive atmospheres, as well as thermal stress, seating face internal stress and combustion gas pressure. It is evident that the working environment of the engine exhaust valve is extremely harsh [3]. The harsh working environment leads to a variety of exhaust valve failure modes, with the most common cause being excessive mechanical loads and high thermal loads resulting in wear of the valve seating face (VSF) [4]. In addition, the combustion pressure causes deflection of the valve head, leading to microscopic sliding motion at the sealing interface, further accelerating the degree of wear. [5, 6]. Chun et al. [7] investigated the impact effects between an engine exhaust valve and a seat insert. The results indicated that impact was the primary cause of seating face wear, while sliding between the two contact pairs accelerated wear. As the valve and valve seat insert are a pair of components in the engine that operate under such harsh conditions when in contact, they must possess high wear resistance and high-temperature stability [8].

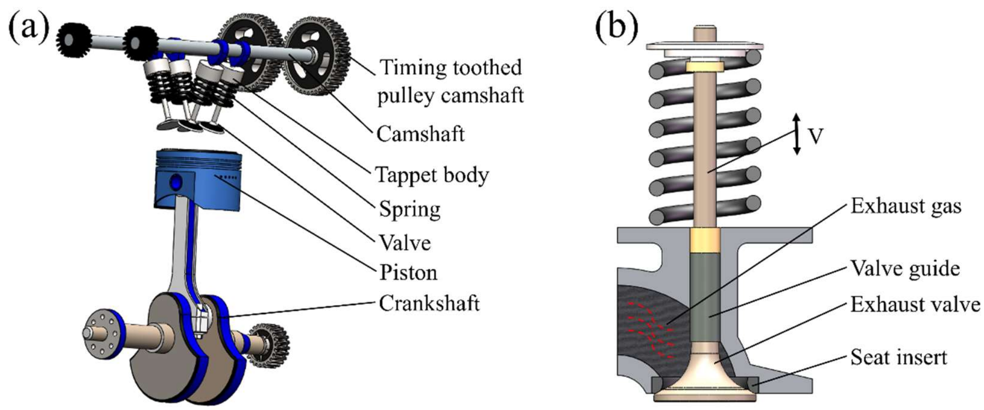

Fig. 1 ICE valve train system: (a) main components, (b) valve working conditions.

The selected valve material must be able to function in harsh working environments. Currently, the most commonly used exhaust valve materials include austenitic heat-resistant steel, iron-nickel-based high-temperature alloys, nickel-based high-temperature alloys, and a small portion of TiAl alloys [9-11]. In this study, Ni30 (also known as NCF3015), a type of iron-nickel-based valve steel, was selected as the valve head material. In order to meet the property requirements, there is an increasing need to introduce surface strengthening treatments to valves to enhance their wear resistance at high temperatures.

Surface treatment technologies have become primary reinforcement measures to enhance the performance of the conical surfaces of engine valves and improve their resistance to high-temperature wear. To meet the demands of the automotive industry, various strengthening techniques have been applied to the surfaces of valves, including nitriding treatment, cone surface cladding, coating technologies, functionally graded composite materials and surface deformation strengthening treatments. Lerman et al. [12] demonstrated that salt bath nitriding of heavy-duty and medium-duty engine valves provided better wear resistance compared to complex valve designs. Wu et al. [13] studied the surface boron diffusion in Al0.1CoCrFeNi high-entropy alloys, finding that as time increased, both the surface hardness and wear resistance improved. Sivakumar et al. [14] used the PVD method to coat the outer surface of traditional single-cylinder diesel engine exhaust valves with H-DLC layers of different thicknesses. Surface analysis showed no measurable wear on the coating and improvement in valve durability. Li et al.[15] combined laser cladding (LC) with laser shock peening (LSP) to prepare 17-4 PH stainless steel. They found a significant reduction in the coefficient of friction (COF) and wear rate of the 17-4 PH clad layer. The improvements in microhardness and wear performance are attributed to the combined effects of grain refinement and dislocation strengthening. Wear-resistant alloy plasma surfacing technology can reduce the wear loss of the VSF, but the failure risk of spalling failure of the surfacing layer and production cost of the surfacing limits its further application [16]. Ram et al. [17-20] synthesized functionally graded A356-Mg_2Si in situ composites using centrifugal casting and conducted an in-depth study of the physical properties of the material. When applied to cylinder liners, dry friction test results indicated that the A356-Mg_2Si composite enhanced the wear resistance of the liners. Sun et al. [21] compared three surface treatment techniques applied to ZL109 aluminum alloy and summarized that dynamic recovery and recrystallization behaviors weakened the effectiveness of strain hardening, while crystal growth reduced the benefits of structural refinement. Additionally, as the temperature increased, the wear mechanisms shifted from abrasion to adhesion and slight oxidative wear.

Surface deformation strengthening, often used in automotive parts, involves causing plastic deformation and work hardening on the material surface, which improves the wear resistance and corrosion resistance of the materials [22, 23]. Previous work by the authors of the study presented here [10] applied ultrasonic surface rolling technology to 23-8N engine valve steel, resulting in significant improvements in wear resistance and fatigue strength.

Among the numerous surface strengthening techniques described in literature and used in industry, surface deformation strengthening treatment of the VSF has the advantages of being a simple operation with low energy consumption and high efficiency, making it a promising method for application. However, there is somewhat limited research on this technique in the published literature; thus is worthy of investigation.

In this study, the Ni30 exhaust valve seating face (VSF) was subjected to plastic deformation by cold upsetting treatment, and the effect on high temperature wear resistance was investigated. The wear mechanisms of the metal sealing surface under high temperature impact were clarified, providing valuable insights for improving the service life of ICE valves. A summary of the work and the research flow chart of this work is shown in Fig. 2.

Fig. 2 The research flow chart.

Fig. 2 The research flow chart.

2. Experimental details and cold upsetting treatment on valve seating face

2.1 Materials

The main chemical compositions of the Ni30 superalloy valve material and seat insert material are presented in Table 1. The seat insert is a commercial ST30 seat insert with high hardness (746.5 $HV_{0.2}$ at 25 °C).

Table 1 Compositions of the engine valve and seat inserts (wt. /%).

	C	Si	V	Cr	Mn	Ni	Mo	Fe	Other

Ni30	0.06	0.08	-	14.50	0.20	31.20	0.75	Bal.	Al:1.8 Ti:2.5 Nb:0.2
Valve seat insert	0.7-1.4	-	13-20	1.5-3.5	-	1.5-3.5	3.5-8.5	Bal.	Cu:10-18 Co:8-15 W:5.5-12

2.2 Cold upsetting treatment on valve seating face

The manufacturing process of engine valves varies according to their material and VSF strengthening methods, but most of them are similar. Recently, Huaiji Dengyue Valve Co., Ltd. proposed a new method of engine valve surface strengthening to improve the fatigue resistance ability [20]. In this study, combined with the existing valve material characteristics and work performance requirements, the focus was on developing the cold upsetting forming process of the Ni30 valve, as presented in Fig. 3. The cold upsetting is a type of forging.

Initially, the solution treatment of the blank valve after electric upsetting dissolves various phases in the alloy into the matrix, improving the toughness and corrosion resistance, eliminating stress and softening the material to obtain a solution treated valve for subsequent cold upsetting treatment. Then, the VSF of the solution treated valve is exposed to the cold upsetting treatment. Subsequently, the valve has aging treatment at high temperature to eliminate the internal stress, stabilize the structure and size, and improve the mechanical properties. Finally, the solution-cold upsetting-aging treated (SCUAT) valve is obtained, and the SCUAT valve component with the required physical size is manufactured by friction welding and a series of finishing processes. By using the same processing technology, a batch of traditional solution-aging treated (SAT) valve components with the same physical size was produced.

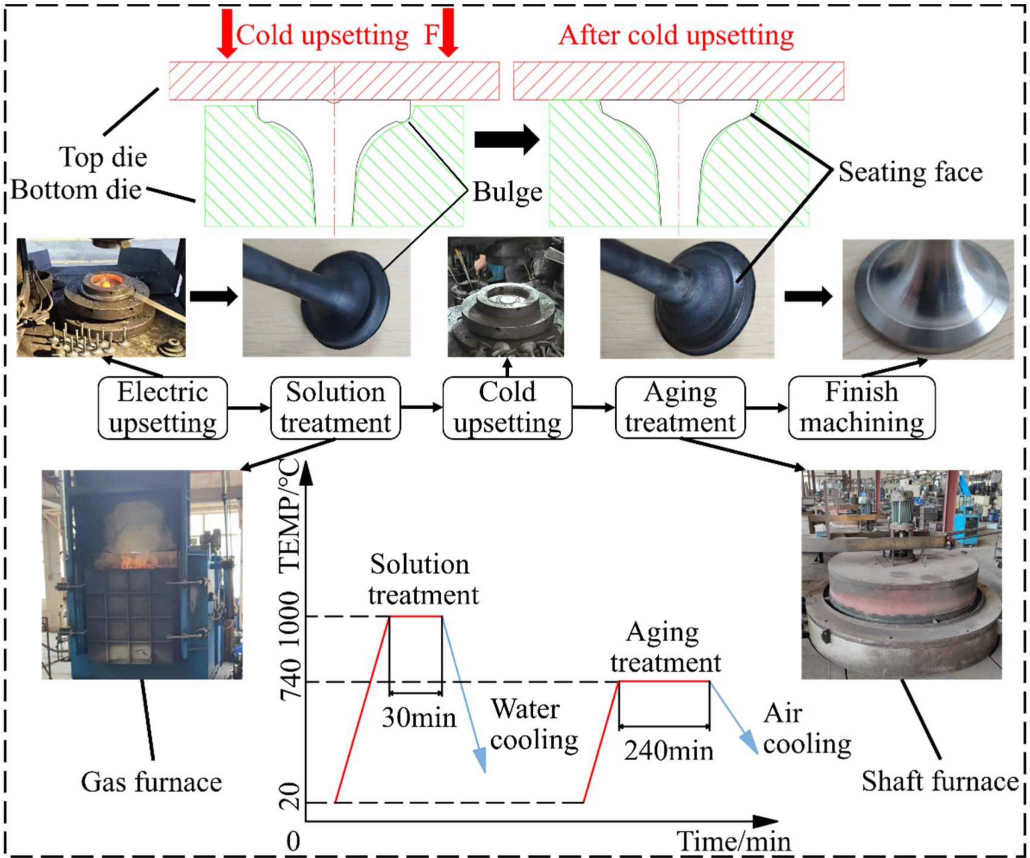

Fig. 3 Main manufacturing processes of engine valve with a special process design of cold upsetting on VSF.

2.3 FEM analysis for cold upsetting treatment of valve seating face

Cold upsetting is a plastic deformation process in which the annular "bulge" of the valve seating face is distributed by an intense and rapid compression, which takes a short time and the material strain rate is at high level. It is difficult to control the deformation flow, and equivalent strain distribution of the material, and it is prone to produce defects such as surface folds and micro-cracks. In reality, it is difficult to observe the deformation process of the material, so numerical simulation is used instead to visualize this process [21]. The simulation of the valve cold upsetting process was conducted using Deform 11.0. The finite element model of the valve cold upsetting process is mainly composed of three parts: top die, bottom die and solution treatment status valve, as presented in Fig. 4.

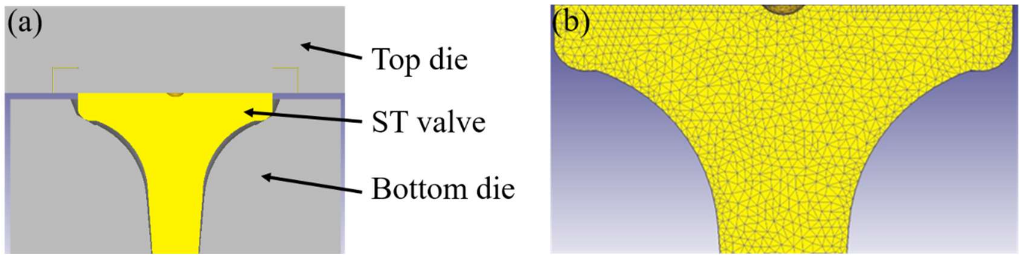

Fig. 4 Numerical simulation: (a) finite element model in Deform software, (b) schematic of element mesh.

The simulation process of valve cold heading pressure is presented in Fig. 5. The annular "bulge" of the VSF of the ST valve in Fig. 5 (a) achieves flattening in Fig. 5 (d) by moving the top die to contact with the bottom die. Throughout the process, the contact area between the valve and the bottom die is mainly concentrated in the "bulge", as presented in Fig. 5 (b). Consequently, the strain is mainly concentrated on the seating face. Properly controlling the size of the bulge avoids defects such as surface wrinkles and micro-cracks after flattening effectively [22]. The main deformation modes of VSF are axial compression and radial extension, as presented in Fig. 5 (c). This process forms a plastic modification layer by compressing the material at the seating face, thereby increasing the wear resistance of the VSF at high temperatures.

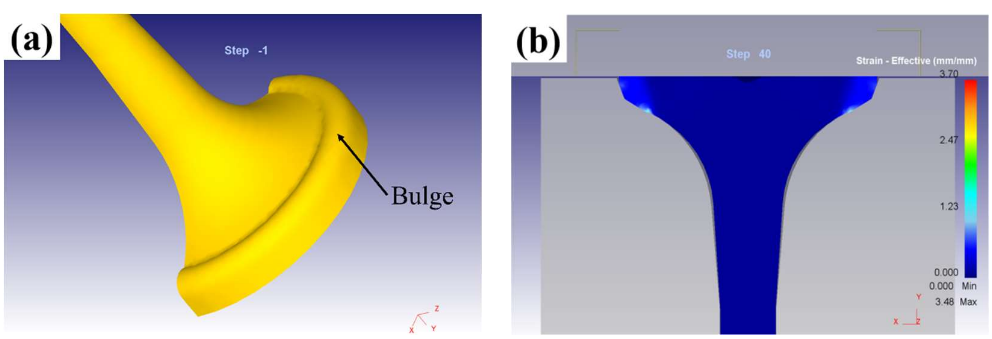

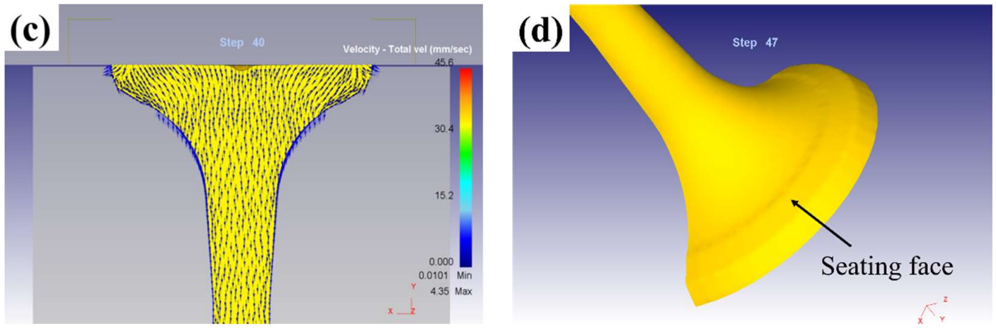

Fig. 5 The simulation results during cold upsetting treatment: (a) annular bulge, (b) strain distribution, (c) velocity distribution, (d) the formed seating face.

2.4 Methods for microstructure characterization

The microstructure of the VSF at each stage of the SAT and SCUAT valve processes was characterized, and the effect of each processing stage on its microstructure and properties was investigated. The test sample extraction location and hardness test point distribution are presented in Fig. 6. Samples were ground and polished using 400-2000 mesh SiC sandpapers and 0.25 µm diamond suspensions. Metallographic structures were observed using an optical microscope (OM; Model DMi8, Leica Microsystems, Germany) after etching with a copper sulphate corrosion solution (5 g $CuSO_4$ + 5 mL H_2SO_4 + 100 mL HCl). Phase analysis was performed using a multi-position automatic injection X-ray diffractometer (XRD; SmartLab, Rigaku Corporation, Japan). The morphologies of the worn surfaces were examined both by scanning electron microscopy (SEM; Quanta 250, FEI, USA), and the elemental compositions of the worn surfaces were investigated using energy-dispersive spectroscopy (EDS) to determine the wear mechanism(s) at elevated temperatures. Electron backscatter diffraction (EBSD) of the VSF was measured using a field emission scanning electron microscope (TESCAN; MIRA3, Symmetry S2, Czechia).

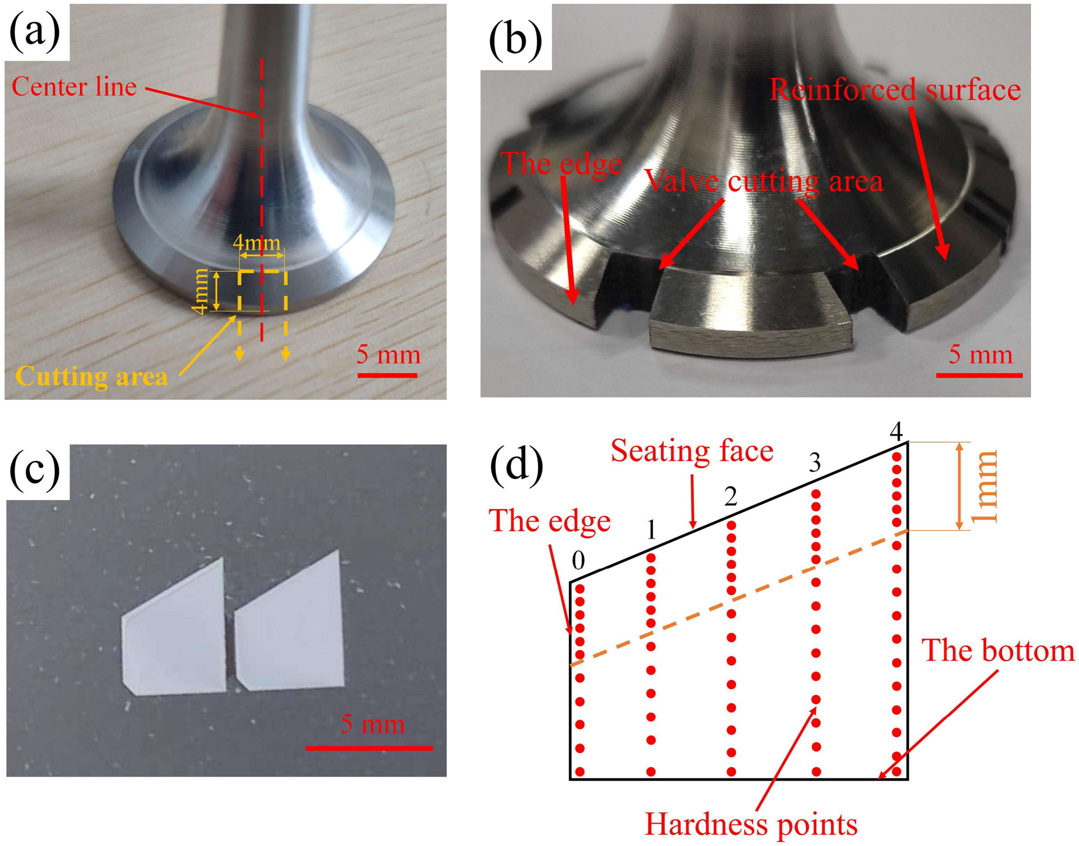

Fig. 6 Sample of VSF: (a) valve microscopic test sample interception position, (b) the valve after cutting, (c) metallographic samples blocks, (d) schematic of hardness test point.

2.5 Bench-top wear test machine and test conditions

High-temperature wear tests of the valves were performed by using a valve-seat insert simulation bench-top wear test machine (FQM-8, Wuhan-WUT, China). A schematic diagram is presented in Fig.7 (a). The geometry of the valve and seat insert is presented in Fig. 7 (b). The valves had a seating face angle of 30°, which is commonly used in applications where combustion products have little or no lubricating properties. The initial contact width of the seat inserts was 2.2 mm [3].

For measuring the wear surface of the valve cone-seat contact pair, a contact profilometer (XC20, Mahr GmbH, Germany) was used to accurately capture the profile information of the wear surface. The testing equipment and schematic for the wear profiles of the valve and seat are illustrated in Fig. 7(c). Before and after the tests, the valve and seat components were placed on an adjustable base, with the scanning probe adjusted to lightly contact the wear surface. The probe was then moved along the predetermined scanning direction to obtain the profile information, scanning every 90° at marked positions.

The morphologies of the worn surfaces and cross-section of the valve and seat insert were examined by scanning electron microscopy (SEM; Quanta 250, FEI, USA), and the elemental compositions of the worn surfaces were investigated using energy-dispersive spectroscopy (EDS) to analyze the wear mechanism at elevated temperatures.

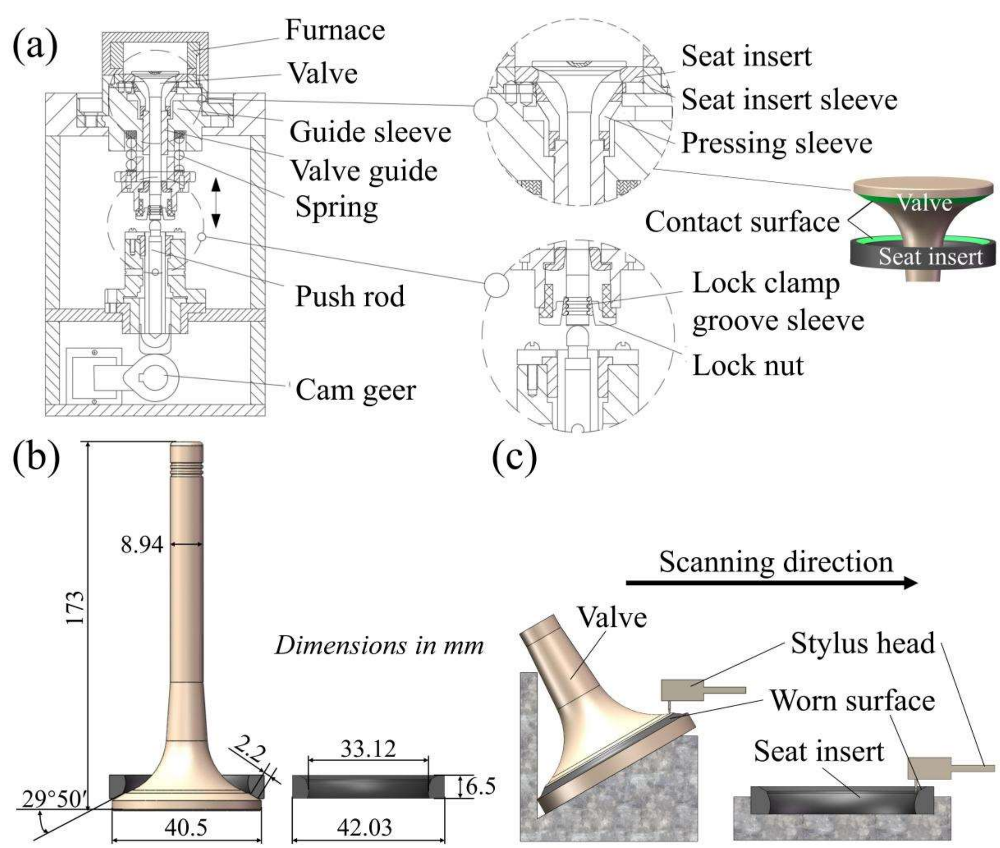

Fig. 7 Bench-top wear test and measurement method: (a) schematic illustration of FQM-8 bench-top wear test machine, (b) valve and seat insert geometry, (c) schematic of worn seating surface measurement through using a profilometer.

The valve recession was measured before and after the bench-top wear tests using specialized measuring fixture. The fixture and the measurement positions are depicted in Fig. 8. The gauge was installed above the circular hole of the fixture, and measurements were taken at intervals of 90° at the outer diameter of the valve's bottom two-thirds. The difference in the average values obtained represents the valve recession after the bench-top wear tests.

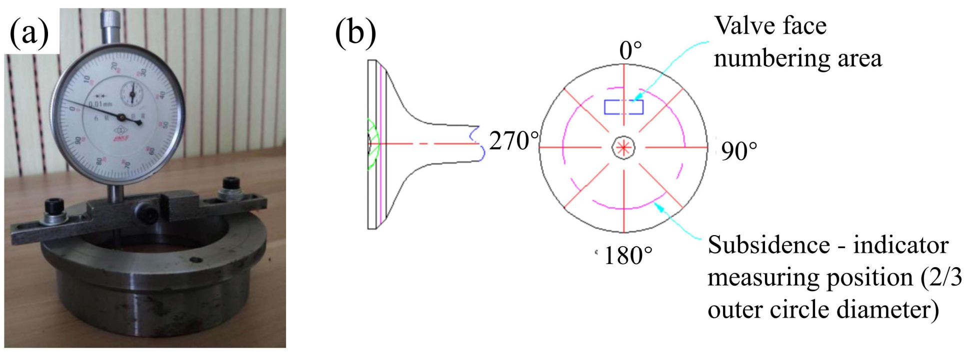

Fig. 8. Valve recession measurement: (a) measuring fixture, (b) measuring position.

With reference to Liu's work [23] and the actual working conditions of the ICE, the test parameters for the wear simulation tester used in this study are presented in Table 2. The SAT valve is designated as test group A, and the SCUAT valve is designated as test group B. In order to ensure a single variable factor, each valve was paired with the same type of seat insert. Lubrication was applied between the valve rod and the valve guide to prevent excessive wear during the vertical movement, which could result in conduit blockage of the valve guide. No lubricating material was added between the valve and the seat insert to ensure dry contact. The axial pre-load was set by the spring deformation length. To simulate the real working conditions of a valve in an engine, the autorotation rate is set to 3.5 rpm.

Each group test was conducted for repeatability by using two samples. As outlined in the testing methods in the text, the wear profile of each valve and valve seat insert was measured four times with an interval of 90° and the average value taken.

Table 2 Bench-top wear test parameters.

Test number	Valve name	Seat insert name	Temperature (°C)	Impact cycles (million)	Speed (times/min)	Axial load (N)	Autorotation rate (rpm)
A-1	V-A-1	VSI-A-1	650	0.5	1400	670	3.5
A-2	V-A-2	VSI-A-2	650	1	1400	670	3.5
A-3	V-A-3	VSI-A-3	650	2	1400	670	3.5
A-4	V-A-4	VSI-A-4	750	0.5	1400	670	3.5
A-5	V-A-5	VSI-A-5	750	1	1400	670	3.5
A-6	V-A-6	VSI-A-6	750	2	1400	670	3.5
B-1	V-B-1	VSI-B-1	650	0.5	1400	670	3.5
B-2	V-B-2	VSI-B-2	650	1	1400	670	3.5
B-3	V-B-3	VSI-B-3	650	2	1400	670	3.5
B-4	V-B-4	VSI-B-4	750	0.5	1400	670	3.5
B-5	V-B-5	VSI-B-5	750	1	1400	670	3.5
B-6	V-B-6	VSI-B-6	750	2	1400	670	3.5

3. Results and discussion

3.1 Microstructure and XRD analysis

The microstructures of the VSF at the two different stages are presented in Fig. 9, with the matrix of these samples exhibiting an austenitic structure. The grains in the SAT stage, shown in Fig. 9 (a), are nearly equal. After the SCUAT, presented in Fig. 9 (b), the grains were crushed and refined after the cold upsetting treatment, resulting in a flattened seating face. Within a certain range, smaller grain sizes alter mechanical properties due to the size effect, which can increase the strength of metals and alloys [24, 25].

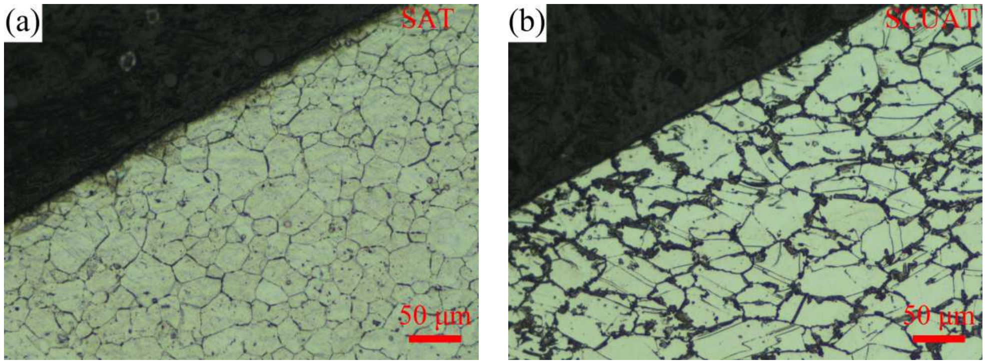

Fig. 9 Microstructures of VSF using optical microscope: (a) SAT, (b) SCUAT.

The results of cross-sectional EBSD observations of the SAT and SCUAT samples are presented in Fig. 10-Fig. 13. The crystal orientation map of the two samples is presented in Fig. 10, where ND represents the normal direction and the equivalent grain diameter (GD) represents the grain size. The grain size of the SAT sample is more uniform compared to that of the SCUAT sample, and the grain shape of the SCUAT sample is more regular. The grain size of the SCUAT sample is polarized with a large amplitude span, indicating significant variation. Many factors are present at the grain boundaries of larger grains. After cold upsetting and crushing, the smaller grains are disordered and irregular in shape. For the SAT sample, the grain size is less than 60 μm, with an average size of 18.80 μm. For the SCUAT sample, the maximum grain size is nearly 100 μm, while the minimum grain size is only about 2 μm. The average grain size is 14.54 μm. Although the SAT sample does not have super-large grains (>60 μm), the SCUAT sample contains a significant proportion of fine grains, resulting in a smaller average grain size overall.

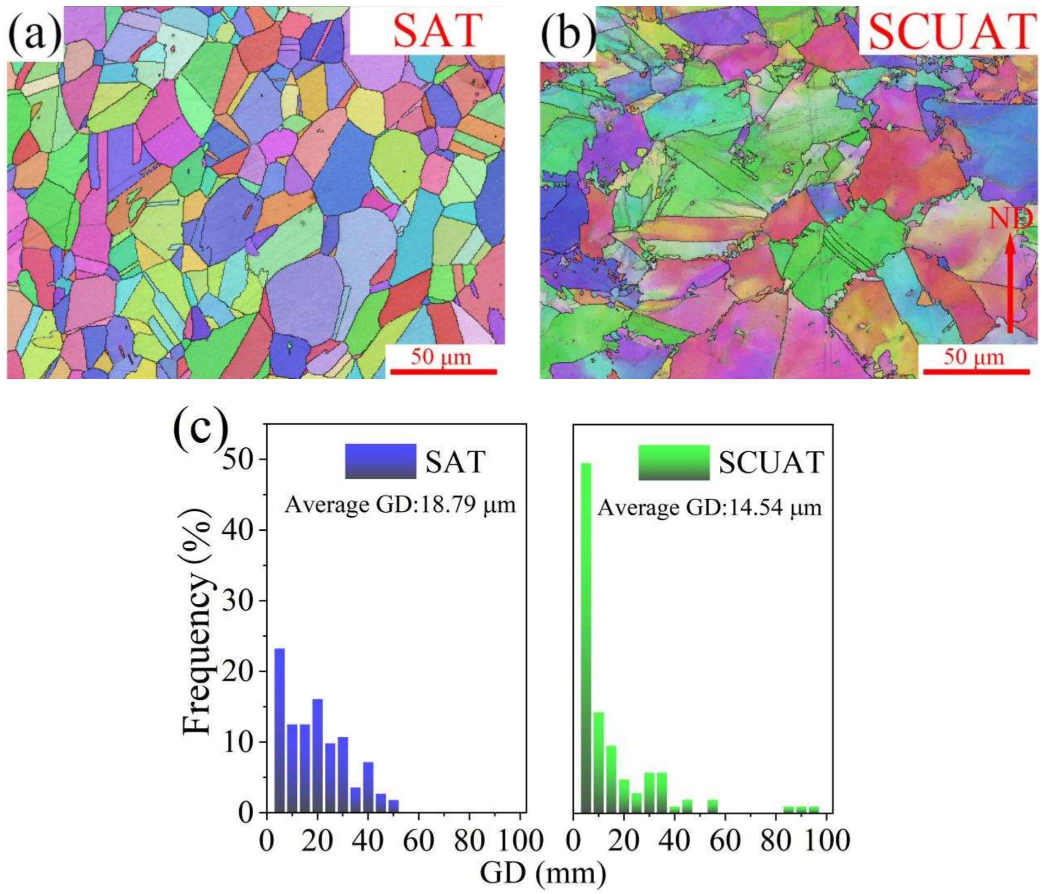

Fig. 10 The crystal orientation map of cross-sectional EBSD observations: (a) SAT, (b) SCUAT, (c) average grain diameter.

The grain boundary angles of the SAT and SCUAT samples are presented in Fig. 11, where low angle grain boundaries (LAGB<15°) are shown in red and high angle grain boundaries (HAGB≥15°) are shown in black [26]. After the cold upsetting treatment, the grains of the VSF were clearly modified. The dislocation accumulation caused by plastic deformation and the grain deformation after aging resulted in changes in the grain boundary angles. For polycrystalline alloys, increasing the proportion of low angle grain boundaries by plastic deformation can reduce the texture difference between grain boundaries and grains and improve the corrosion resistance of the alloys [27]. The average grain boundary angle of the SAT sample is 48.36 °, while that of the SCUAT sample is 9.85°. The grain boundary angle of the VSF after cold upsetting treatment is significantly changed.

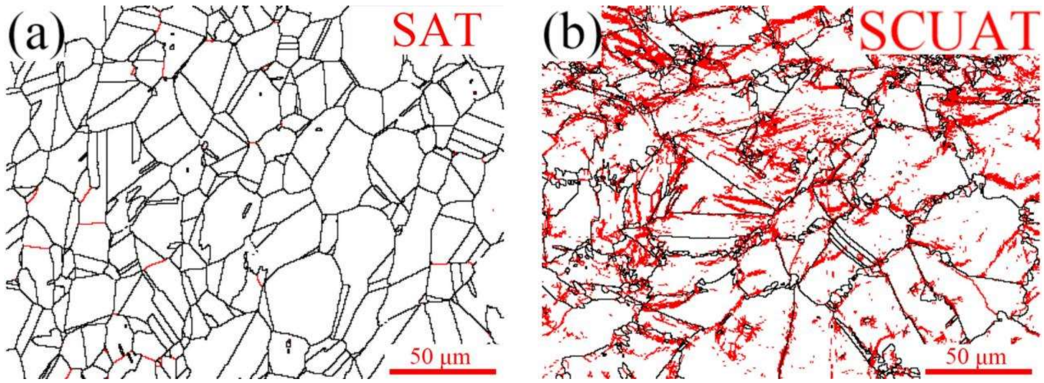

Fig. 11 The grain boundary angle of cross-sectional EBSD observations:(a) SAT, (b) SCUAT, (c) average AGB.

Local misorientation is calculated by determining the orientation difference between each small area in the selected region and its surrounding areas, and the average misorientation is assigned to the central area of the selected region [28]. In order to avoid statistical local misorientation at grain boundaries, the local misorientation within a 5° range for the SAT and SCUAT samples is presented in Fig. 12, where blue indicates small local misorientation and yellow-green indicates large local misorientation. The SAT sample predominantly appears blue, indicating that the local misorientation within the SAT sample VSF material is at a low level. In contrast, the SCUAT sample shows a significant amount of yellow-green, indicating a substantial increase in local misorientation between the grains on the VSF of the SCUAT sample. This increase is attributed to the cold upsetting treatment, which enhances the plastic deformation of the VSF material, generating numerous dislocations and substructures within the material and thereby increasing local misorientation [10].

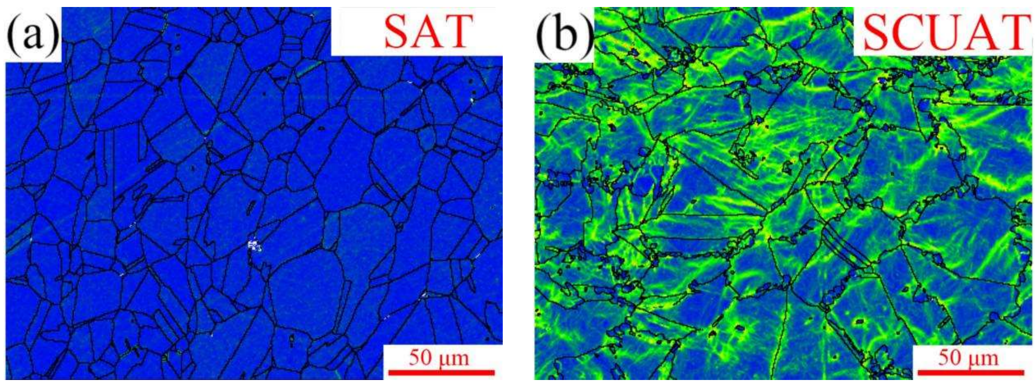

Fig. 12 The local misorientation of cross-sectional EBSD observations: (a) SAT, (b) SCUAT, (c) local misorientation.

The polar diagram of a crystal face can be obtained by the polar projection of all equivalent crystal faces of a certain crystal face of a material, which is usually used to express the three-dimensional spatial distribution of the crystal faces and crystal directions of the important crystal faces. The darker the color, the higher the polar density, indicating a preferred orientation of the crystal faces and directions [29]. The polar diagrams of {100}, {110} and {111} faces of

SAT and SCUAT samples are presented in Fig. 13. The strength distribution of the two samples is not equal, both have texture, but the polar density of the SAT sample is relatively higher. The texture orientation of the SCUAT sample after cold upsetting treatment was changed to some extent, and the polar density of the SCUAT sample was lower than that of the SAT sample.

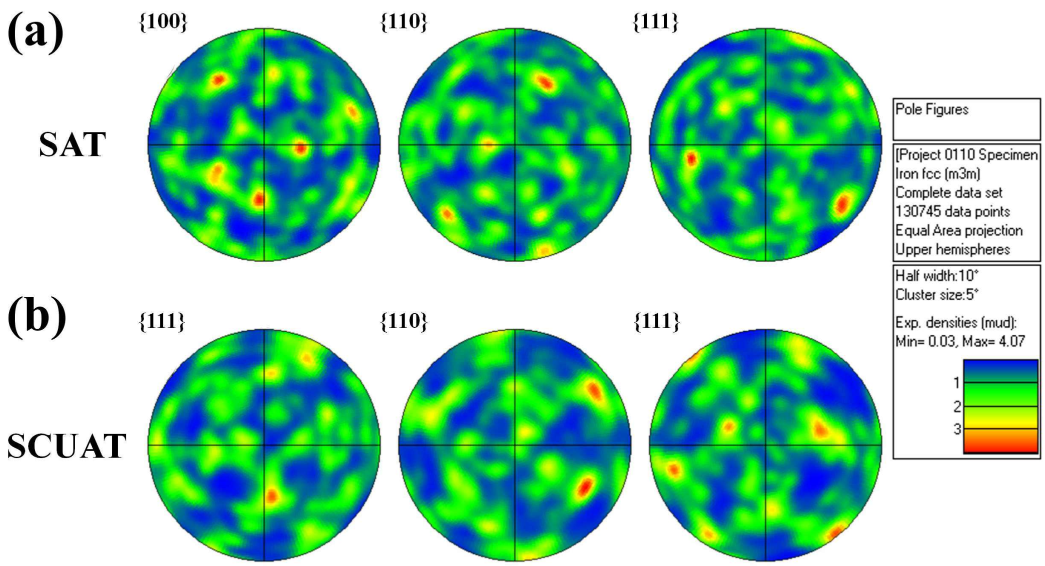

Fig. 13 The polar diagrams of VSF cross-sectional EBSD observations: (a) SAT, (b) SCUAT.

In order to have a more intuitive understanding of the difference in microstructure of the VSF material in the SAT and SCUAT valves, the EBSD results described above were quantitatively calculated. The obtained average grain size ($\bar{d}$), average grain boundary angle ($\bar{\theta}$), proportion of small grain boundary (*f*), proportion of large grain boundary (1-*f*), average angle of low grain boundary ($\bar{\theta}_{\mathrm{LAGB}}$) and average angle of high grain boundary ($\bar{\theta}_{\mathrm{HAGB}}$) are listed in Table 3.

Table 3 Grain information statistics of SAT and SCUAT samples.

Type	All		<15° (LAGB)		≥15° (HAGB)	
	$\bar{d}$ (μm)	$\bar{\theta}$ (°)	f	$\bar{\theta}_{LAGB}$	1-f	$\bar{\theta}_{HAGB}$
SAT	18.80	48.36	0.04	6.26	0.96	49.95
SCUAT	14.54	9.85	0.84	2.07	0.16	49.91

XRD patterns of SAT and SCUAT samples are presented in Fig. 14, indicating that the structure was composed of the γ phase and the γ' phase. The γ' phase composed of Ni_3 (Ti, Al) is the main strengthening phase. Its morphology and size play an essential role in the properties of materials [30].

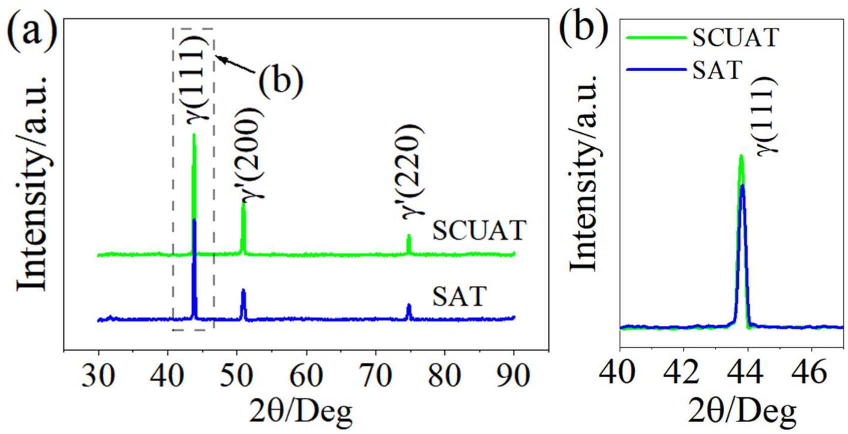

Fig. 14 XRD patterns of SAT and SCUAT samples: (a) the overall curve, (b) enlargement of local degrees.

3.2 Microhardness distribution analysis

Microhardness patterns of the VSF in the SAT and SCUAT samples are presented in Fig. 15. The SCUAT sample shows an increase in hardness of 60 $HV_{0.2}$ over the SAT sample. Generally, higher hardness means better wear resistance, but higher hardness does not necessarily mean better wear resistance, because materials with high hardness are prone to peeling off during wear, which can cause severe damage to the material matrix [37]. The effect of cold upsetting treatment on the high-temperature wear resistance of the valve will be studied later.

Fig. 15 Microhardness distribution of VSF: (a) SAT, (b) SCUAT.

3.3 Wear resistance of valves

3.3.1 Wear scar of valve seating face

The valves before and after the high-temperature wear test are presented in Fig. 16. The surface wear loss of the contact pair of the valve-seat insert is a complex process affected by materials, test condition and time (impact cycles). Before the test, the surface of the sample was smooth and showed the color of metal material. After the high-temperature wear test, the surface color of the valves changed to a certain extent, and the VSF displayed macroscopical wear scar caused by impact.

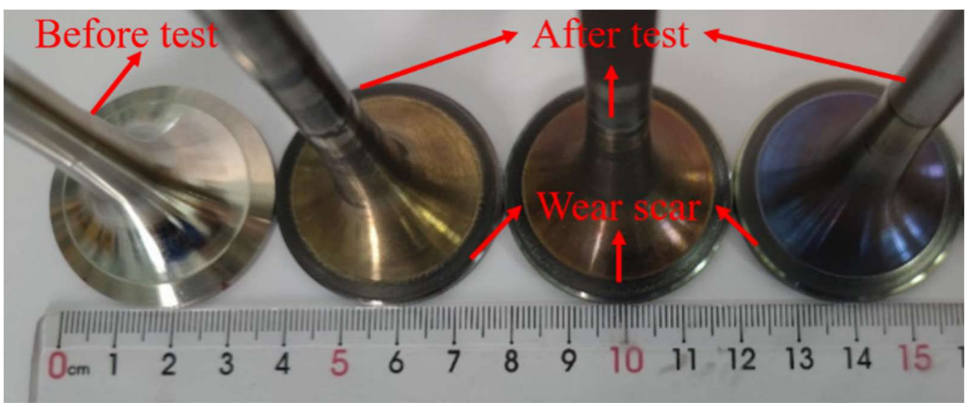

Fig. 16 The valves components before and after the high-temperature bench-top wear tests.

Images of the seating face of the V-A-5 and V-B-5 after one million impact cycles at 750 °C are presented in Fig. 17 (a) and Fig. 17 (b), respectively. Based on the 2D wear scar profiles, the wear scar area was then calculated. Fig. 17 (c) reveals the wear scar area of the VSF after a wear test, respectively. The error bars in the figure represent the standard deviation of the wear scar information. Both of the two types valves, the wear scar area increased rapidly with increasing number of impact cycles between the valve and the seat insert. When the axial force is constant, the contact area between the valve and the valve seat insert increases with the wear process. This leads to a reduction in impact stress in the contact area over time, which in turn decreases the growth rate of the wear scar area. Under the same bench-top wear test conditions, the wear scar area of the SCUAT valve was smaller than that of the SAT valve. Compared to the SAT valve, the wear scar area of the SCUAT valve was decreased from 0.377 mm^2 to 0.246 mm^2 after two million impact cycles at 650 °C, representing a reduction of 34.75%. However, temperature had a significant effect on material properties. After the same number of impact cycles, the width and area of valve wear scar at 650 °C were larger than those at 750 °C, with the scar area at 650 °C about three times larger than those at 750 °C. The wear test results showed that the high temperature wear resistance of the SCUAT valve was better than that of the SAT valve. This could be attributed to the increased hardness and dislocation density of the VSF due to cold upsetting treatment, which increased its wear resistance. Although with an increase in temperature, the hardness of Ni30 valve steel decreases [3, 31], the wear loss of the valves at 650 °C was higher than at 750 °C after the same number of impact cycles. This discrepancy suggests that factors other than hardness, such as the wear mechanism, play a significant role, which will be discussed in Section 3.4.

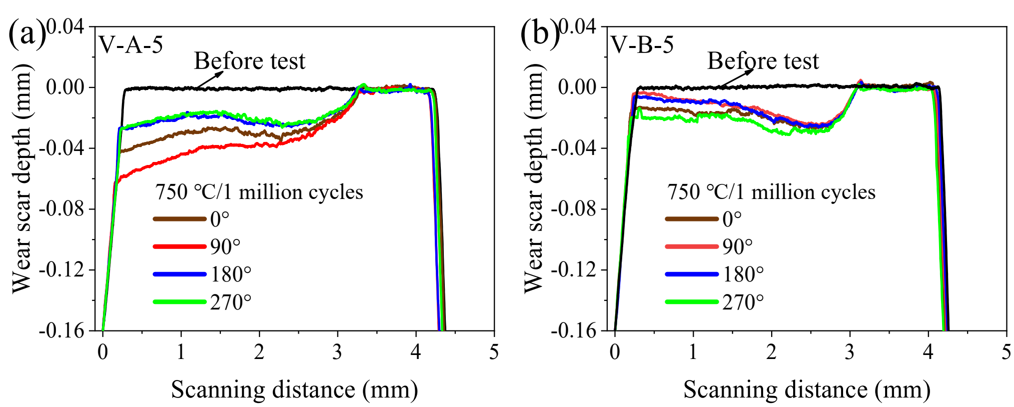

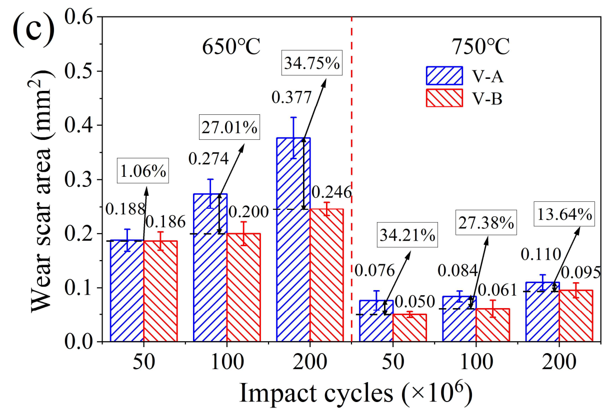

Fig. 17 Wear scar of VSF: (a) The wear scar profile of V-A-5, (b) The wear scar profile of V-B-5, (c) Wear scar area of the valve.

3.3.2 Wear scar of seat insert

The wear scar profiles of the VSI-B-3 seating face after a wear test and the average value of wear scar area of all seat inserts are presented in Fig. 18 (a) and Fig. 18 (b), respectively. The error bars represent the standard deviation of the calculated wear scar areas. The results show that the material loss of the VSI-A seat insert was less than that of the VSI-B seat insert at the same temperature for fewer than one million impact cycles. However, the magnitude of material loss tended to be the same when the impact cycles were increased by two million.

The wear loss of seat inserts under bench-top wear tests was similar to that of valves. After the same number of impact cycles, the wear loss at 650 ℃ was higher than that at 750 ℃. But the wear loss of the seat insert gave a higher variation range at different measurement points at 650 ℃, indicating less uniform wear around the circumference of the seat. The valve head material in contact with the seat insert is Ni30 valve steel, and the temperature and impact cycles were the main factors affecting the wear loss of the seat insert.

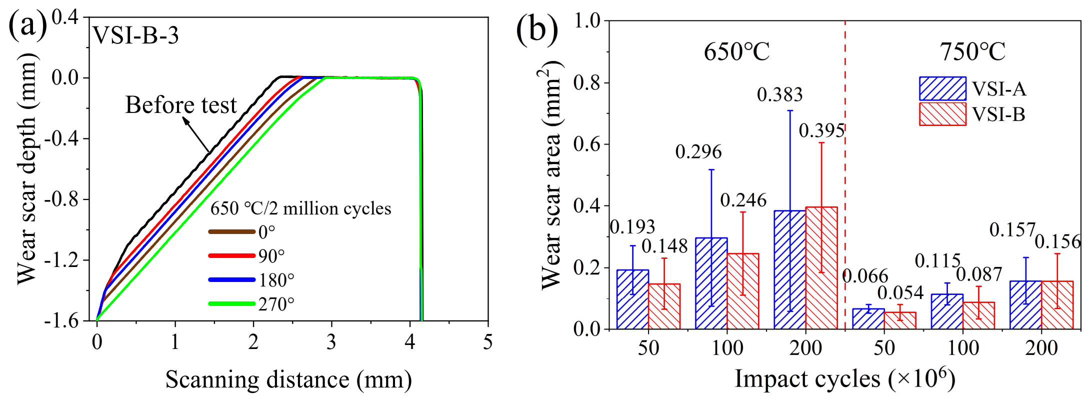

Fig. 18 Wear scar of seat insert: (a) the wear scar profile of VSI-B-3, (b) wear scar area of the seat insert.

3.3.3 Combined wear of the valve and seat insert contact pair

For the evaluation of the wear resistance of the contact pair of valve-seat insert, the wear loss of both parts should be calculated. This is particularly important when evaluating surface treatments that modify hardness as a previously compatible pair might subsequently produce excessive wear of a single part, leading to the failure of the combined contact pair, due to one of the pair now being excessively hard (or soft) relative to the other.

The total wear area of all contact pairs is presented in Fig. 19. During the wear test under the condition of a half million impact cycles, the wear scar area of the valve was mostly higher than that of seat insert. However, when the impact cycles reached one million or more, the wear scar area of the seat insert became higher than that of valve. Compared to the total wear loss of the SCUAT contact pairs and the SAT contact pairs, the SCUAT contact pairs exhibited a decrease of up to 26.76%.

A schematic of valve recession is presented in Fig. 19 (a), and the valve recession followed the same variation trend of total wear of contact pairs, as presented in Fig. 19 (b). Due to the dry sliding, the rate of valve recession was higher than that in an actual engine. In the actual running engine, combustible gases typically exist in the form of fine mist-like liquid particles, which can act as lubricants between contact surfaces. Therefore, due to the presence of combustible gases, the wear on the valve seat and valve gasket in real-world applications is slower compared to the wear observed in this experiment[32]. The results showed that valve recession at 650 ℃ was more serious than that at 750 ℃, and valve recession of SAT was also more than SCUAT valves. This showed the same trend as the previous results, which further proved that the SCUAT valve had better wear resistance at high temperatures, as presented in Fig. 20.

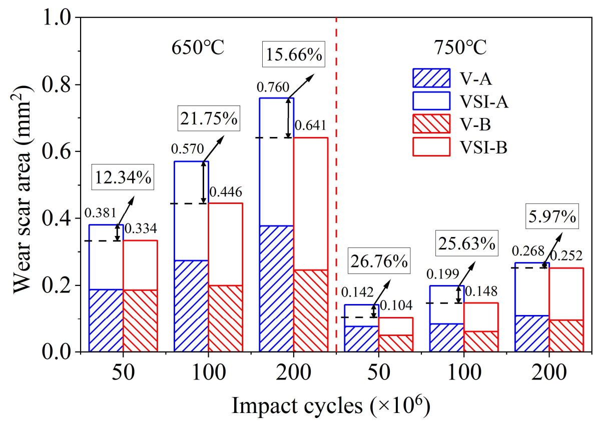

Fig. 19 Total wear area of contact pairs of valve and valve seat insert.

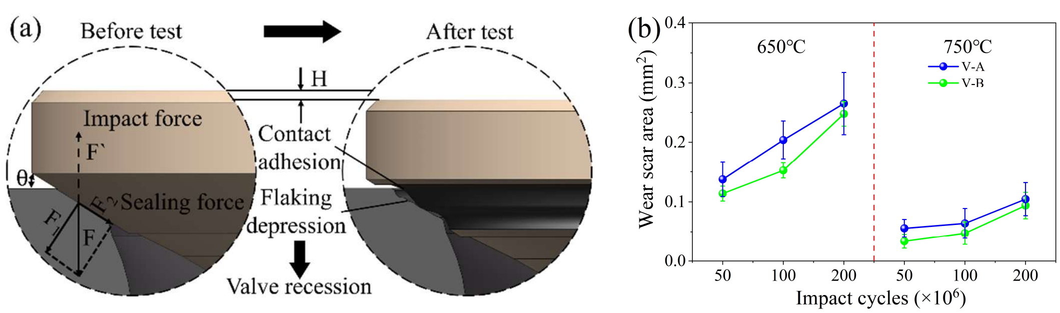

Fig. 20 Valve recession results after bench-top wear test: (a) schematic diagram of valve recession, (b) valve recession results of valve samples.

3.4 Worn surface morphology and wear mechanism

3.4.1 Worn surface morphology of valve seating face

Surface fragmentation and material transfer occurred during the wear test as the surfaces underwent a complicated process of mixing, compacting and smearing under the normal load and friction force between the contacts with the further sliding. Figs. 21-24 present the worn surfaces of the VSF of V-A-3, V-B-3, V-A-6 and V-B-6 under two million impact cycles, respectively. The EDS results of the areas on the VSF are presented in Table 4.

The test temperature of V-A-3 and V-B-3 was 650 ℃, V-A-6 and V-B-6 was 750 ℃. For instance, Fig. 21 presents the VSF worn surface of V-A-3. The black line is the dividing line between the worn area and the non-worn area. Based on the degree of wear, it is divided into area A with severe wear and area B with slight wear, as presented in Fig. 21 (a). The oxide film caused by high-temperature test conditions was unevenly distributed in the worn area. It can be observed from Fig. 21 (b) that a large area is covered with a typical bonding layer and debris. Meanwhile, compared to the non-worn area of the VSF, V, Co and Cu are also detected on the worn area (Table 4), indicating that the seat insert material is transferred to the VSF and that the adhesion is an oxygen-rich compound. Mascarenhas et al. also reported a similar phenomenon [33]. Under high-frequency impact loads, the plastic deformation of the material on the valve seat surface gradually accumulates, leading to performance degradation. This accumulation results in grooves on the worn surface and the formation of microcracks, as shown in Fig. 21(c). As the loading impact continues, the microcracks propagate further into the surrounding area, eventually causing layered spalling of the surface material, as shown in Fig. 21(d). Wear on the inside of the wear area was mainly caused by micro-sliding of valve and

VSI contact surfaces, and there is a large area of oxide film in this area, as presented in Fig. 21 (d). The material shows spalling behavior, and the predominant wear mechanism could be classified into fatigue wear.

In comparison, the V-B-3 valve, as presented in Fig 22, underwent cold upsetting treatment. The SCUAT valve surface exhibits smaller average grain size and higher surface and subsurface hardness. Additionally, cold upsetting increases the dislocation density in the grains of the SCUAT valve, which improve the resistance of crack initiation, and inhibit crack propagation rate. [34]. The contact area does not exhibit as large and deep spalling pits as the V-A-3 valve, thus reducing the degree of wear on the VSF and showing better high-temperature wear resistance. The content of V, Co and Cu elements in the V-3 area is higher than that in the V-2 area (Table 4), which further proves that the wear of area B is less than that of area A. There is also evidence of adhesive wear and fatigue wear.

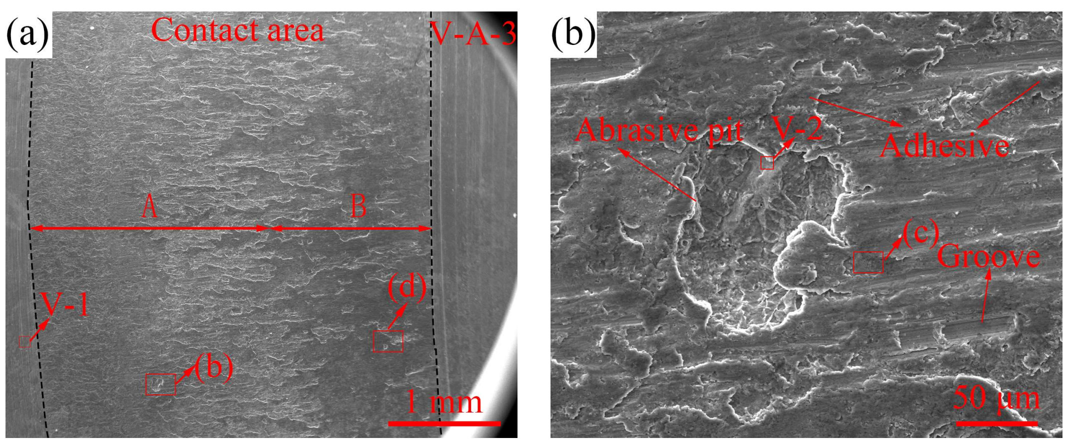

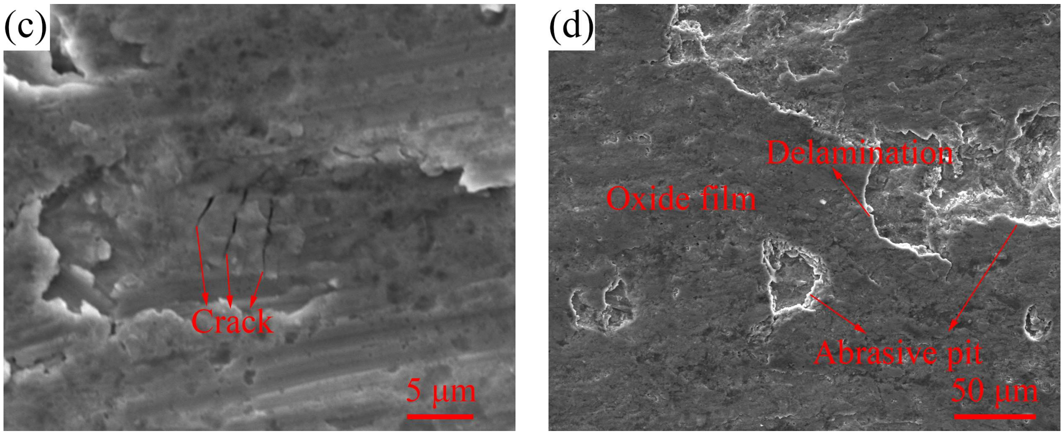

Fig. 21 The wear morphology of V-A-3. (a) worn surface and EDS test area V-1, (b) enlarged view of worn surface and EDS test area V-2, (c) crack amplification, (d) delamination crater.

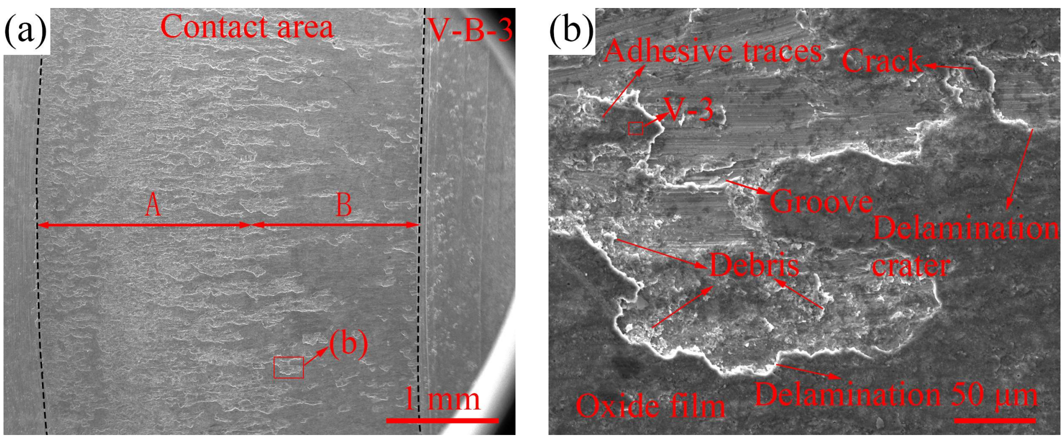

Fig. 22 The wear morphology of V-B-3: (a) worn surface, (b) enlarged view of worn surface and EDS test area V-3.

The VSF worn surface morphology of V-A-6 is presented in Fig. 23. At 750 ℃, the surface material does not show as many noticeable spalling pits as at 650 ℃, but there are noticeable traces of plastic flow and large grooves, indicating a lower degree of wear. According to EDS test results (Table 4), the oxygen content in the V-4 area is higher, signifying that the oxidation degree of the material is at high level. Additionally, the presence of V, Co and Cu elements indicates that material transfer occurs during the wear process, and the wear mechanism is mainly adhesive wear and oxidation wear.

In comparison, the V-B-6 valve, as shown in Fig. 24, reveals a dense oxide layer in area B.

There are a large number of adhesion traces on the surface of area A, which is due to the fact that the hardness of Ni30 superalloy will gradually decrease uniformly with rising temperature, which increases abruptly after about 650 °C. Under the condition of 750 °C, the material becomes softened, making it easier to adhere to the worn surface [31]. The sealing force is generated by the high-frequency impact action, and the surface of the material generates a plastic flow to form grooves. The valve moves along the contact, resulting in skid marks. The positive force of the vertical contact surface creates cracks in the adhesive layer, which eventually causes the adhesive layer to fall off, leading to renewed impact wear on the matrix. As the cold upsetting treatment improved the performance of the VSF, the area and depth of the stratified pit in the B area are smaller, and the oxide layer is denser at 750 °C than at 650 °C. According to the calculation model of oxidative wear proposed by Quinn [35], the wear rate is closely related to the critical thickness of the oxide film. Due to the high hardness of the seat ring, the oxide film of the material is more likely to fall off during initial wear impact at 650 °C. Higher temperatures accelerate the formation of the oxide film. Although the mechanical properties of the material will be reduced by the increase in temperature, this negative impact is outweighed by the positive effects of seat hardness and oxide film. Consequently, the wear of the valve disc cone under 650 °C condition is more serious. EDS detection results (Table 4) in the V-5 area still showed high oxygen content and the presence of V, Co, and Cu elements, indicating material transfer from the seat insert, and the predominant wear mechanism can therefore be classified as adhesive wear.

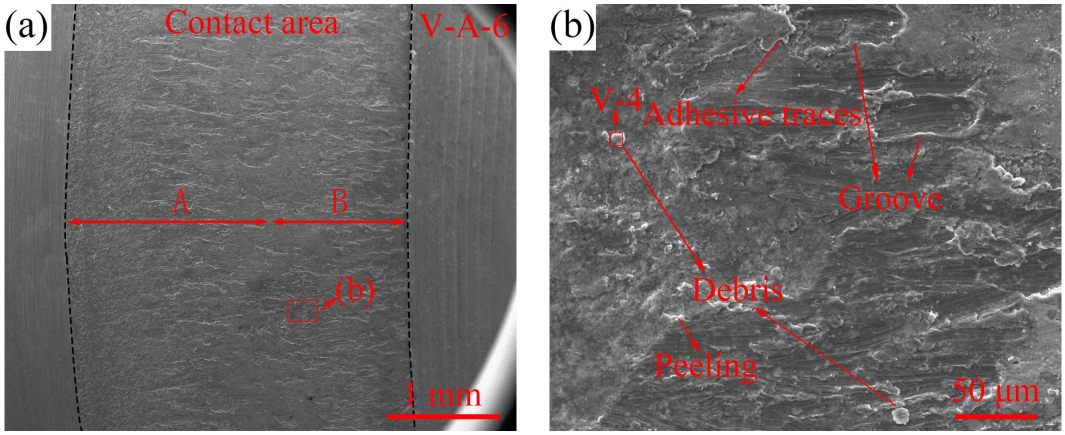

Fig. 23 The wear morphology of V-A-6: (a) worn surface, (b) enlarged view of worn surface and EDS test area V-4.

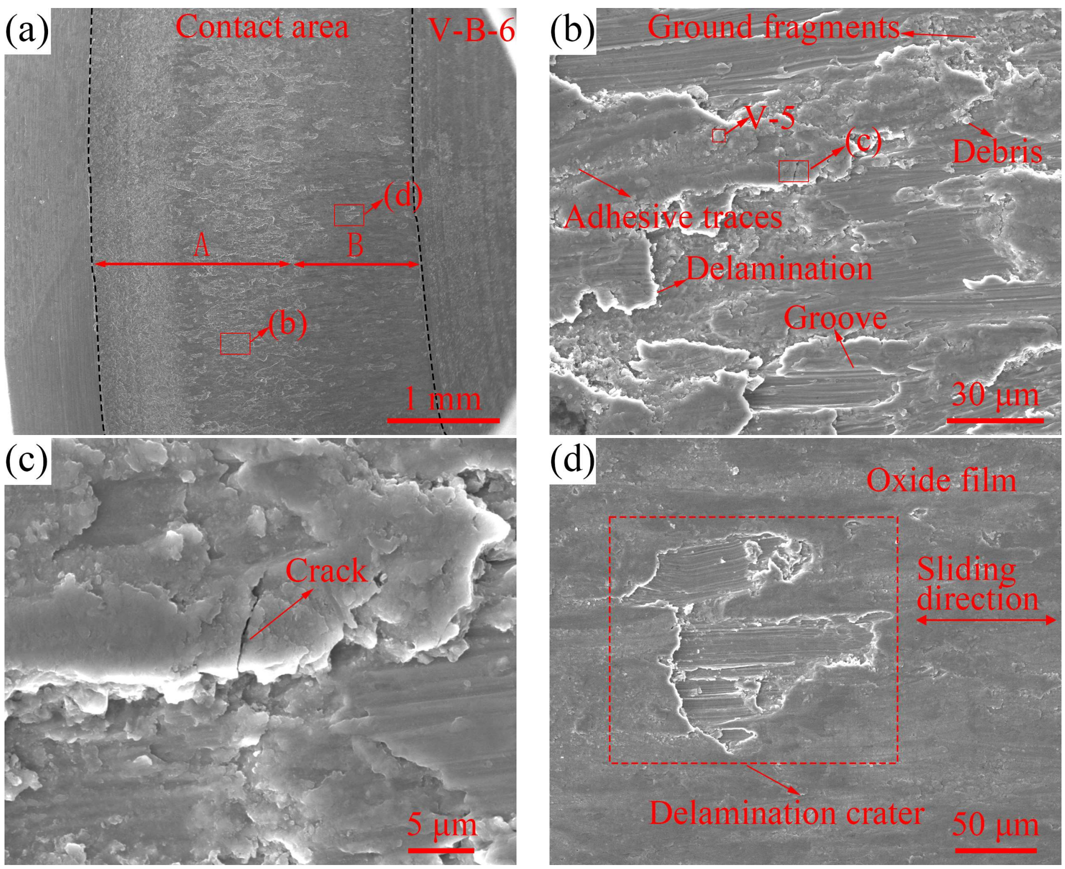

Fig. 24 The wear morphology of V-B-6: (a) worn surface, (b) enlarged view of worn surface and EDS test area V-5, (c) crack amplification, (d) sliding direction.

Table 4 EDS results of the areas on valve seating surface (wt. /%).

Area	C	O	Al	Ti	V	Cr	Fe	Co	Ni	Cu	Mo	Nb
V-1	5.40	2.45	1.93	2.84	-	13.71	43.47	-	28.58	-	0.84	0.78

V-2	6.05	13.08	1.20	1.58	3.08	10.81	40.06	1.30	15.40	3.00	4.44	-
V-3	11.25	21.38	0.57	0.67	6.31	7.44	32.40	1.78	7.24	4.90	6.06	-
V-4	5.43	30.51	0.52	0.38	5.03	5.86	28.85	2.57	7.79	8.40	4.67	-
V-5	6.78	20.56	1.00	1.73	5.81	9.41	31.86	0.87	10.06	3.01	8.91	-

3.4.2 Cross-section morphology of valve seating face

The cross-section morphology of VSF and EDS test results from line scanning are presented in Fig. 25. The figure illustrates that the abrasive adhesion layer formed on the valve disc cone material, treated by cold heading pressure, is more resistant to cracking under the same working conditions. This results in the oxide film of the V-B-3 and V-B-6 valves being more symmetrical than that of the V-A-3 and V-A-6 valves. At 750 °C, the oxide films on the valve worn surface are thicker than that at 650 °C, providing stronger protection to the matrix material and resulting in relatively lighter wear at 750 °C. Some studies have also found that within a certain test temperature range, the material shows more significant wear protection friction film at higher temperatures, resulting in a reduction in the amount of wear [36, 37].

According to the EDS test results, mechanical mixing occurs between valve and seat materials during high-temperature wear. The oxide film contains increased levels of O, Co and Cu elements, indicating the transfer of seat materials due to high-temperature oxidation and wear. When the line is swept between the matrix and the oxide film, the contents of Fe, Ni and Cr elements begin to increase. The amount of O, Co and Cu decreases gradually. This further confirms that the wear mechanisms of the valve disc cone involve a combination of adhesive wear, oxidation wear and fatigue wear.

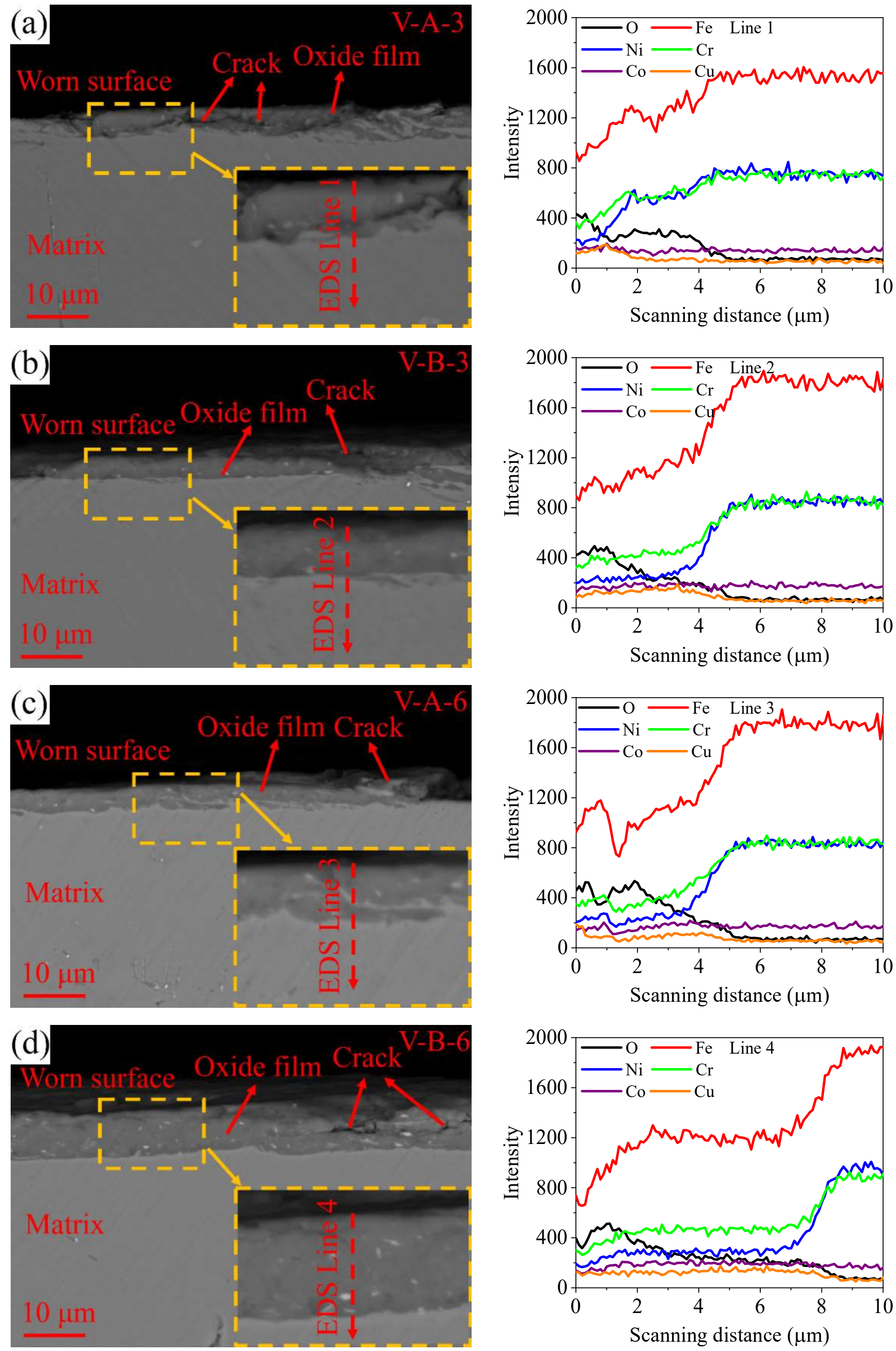

Fig. 25 Cross-section morphology and EDS results of VSF: (a) V-A-3, (b) V-B-3, (c) V-A-6, (d) V-B-6.

3.4.3 Worn surface morphology of seat insert

The wear of the valve-seat insert contact pair mainly comes from the impact and slip of the valve against the seat insert [5]. The hardness of the seat insert is much higher than that of the valve. With the increase of impact cycles, the valve head material is compacted into a thin layer and adhered to the surface of the seat insert. Fig. 26 presents the worn surface of the VSI-A-3 and VSI-B-3 seat insert. The EDS results of the areas on the seat insert face are detailed in Table 5. As can be seen in Fig. 26 (a), the overall wear on the worn surface appears relatively uniform, with uneven abrasive pits. Many cracks can be seen within and around the abrasive pits as presented in Fig. 26 (b). This is due to the VSI ring being manufactured from various metal powders through sintering. The matrix of the material is made up of metal particles of uneven size, resulting in numerous small void gaps and poor plasticity. With the expansion of cracks, the bulk of the material is eventually spalled off, forming abrasive pits. Comparatively, Fig. 26 (c) and Fig. 26 (d) show the material on the worn surface of the seat ring cracks after being impacted. The molten bonded metal particles show massive spalling with the increase of impact cycles. According to EDS test results (Table 5), high-temperature impact wear leads to a mixture of materials on the valve-seat contact surface. The S-2 and S-3 areas have a higher oxygen content and the presence of Ti and Al elements, which are not found in the S-1 area. Under this working condition, the worn surface of the VSI ring has more spalling pits, indicating that the primary wear mechanism is fatigue wear.

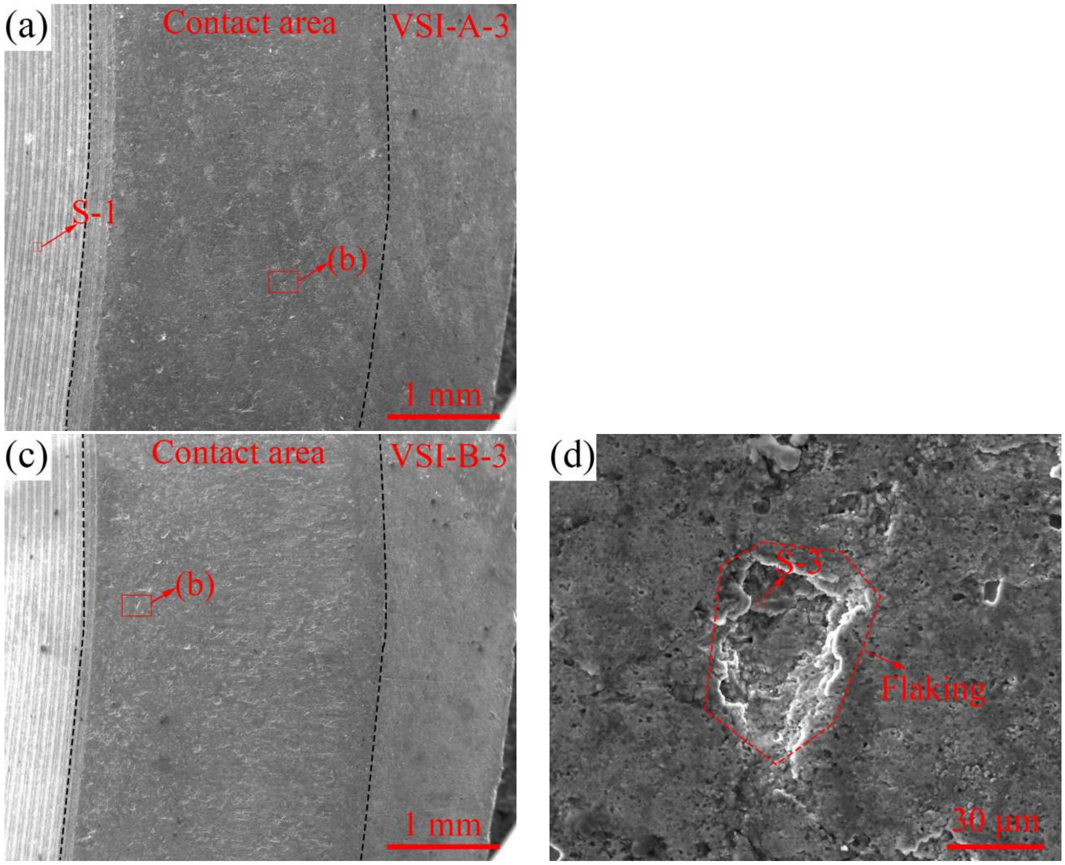

Fig. 26 Worn surface morphology of valve seat insert seating face: (a) worn surface of VSI-A-3 and EDS test area S-1, (b) enlarged view of VSI-A-3 worn surface and EDS test area S-2, (c) worn surface of VSI-B-3, (d) enlarged view of VSI-B-3 worn surface and EDS test area S-3.

The worn surface morphology of VSI-A-6 and VSI-B-6 are presented in Fig. 27. As can be seen in Fig. 27 (b), a small area of abrasive pits appears on the worn surface of the VSI-A-6, with the degree of spalling reduced compared to that observed at 650 °C. Additionally, more adhesive traces are present. The worn surface of the VSI-B-6 has a wide range of adhesive layers, as presented in Fig. 27 (d). The oxygen content and the content of Al, Ti and Nb elements are high in the S-5 area, indicating that the adhesive material consists of a mixture of materials that fall off due to the impact of the valve and VSI contact surface. Although the bonding layer and oxide film may remove the matrix material of the contact surfaces of the valve and seat insert when it is removed by impact, they also avoid the direct collision between the valve and the seat matrix. This reduction in direct impact helps to minimize damage to the matrix, thus reducing the overall wear of the valve components.

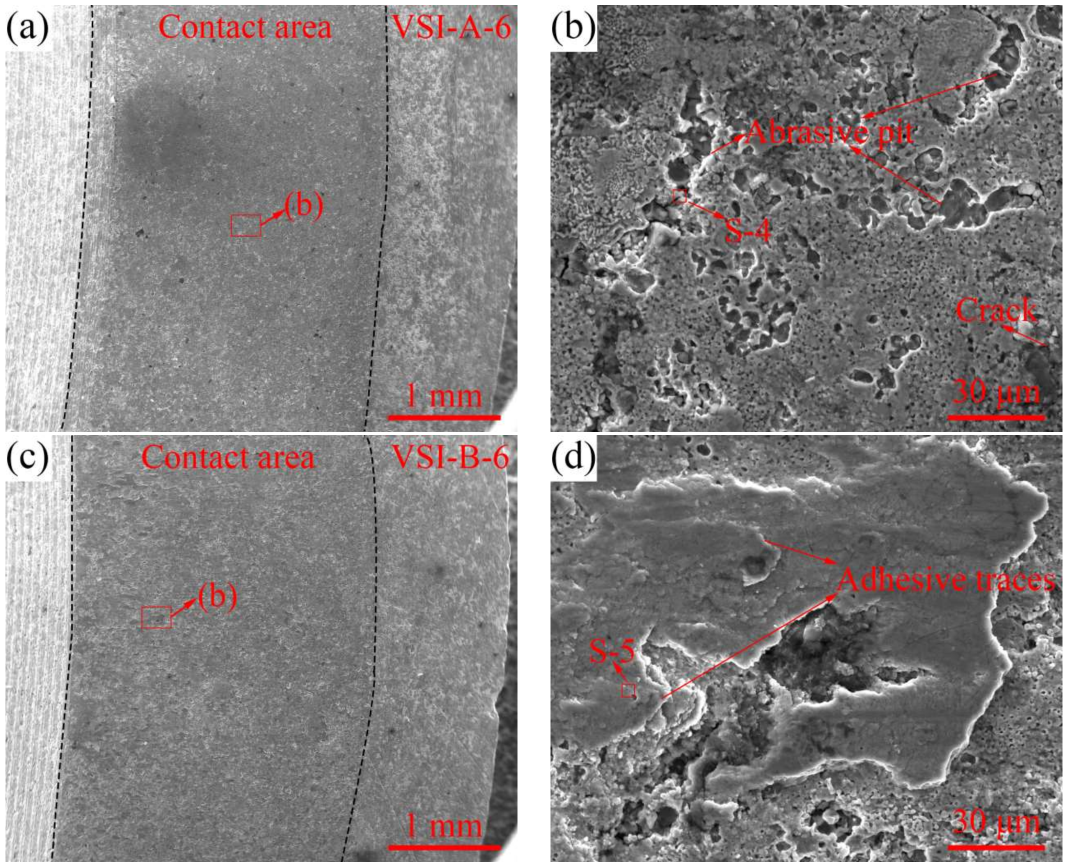

Fig. 27 Worn surface morphology of valve seat insert seating face: (a) worn surface of VSI-A-6, (b) enlarged view of VSI-A-6 worn surface and EDS test area S-4, (c) worn surface of VSI-B-6 worn surface, (d) enlarged view of VSI-B-6 worn surface and EDS test area S-5.

Table 5 EDS results of the areas on valve seat insert seating face (wt. /%).

Area	C	O	Al	Ti	V	Cr	Fe	Co	Ni	Cu	Mo	Nb	W
S-1	8.10	7.65	-	-	11.25	5.54	38.30	4.67	1.86	7.21	9.46	-	5.96
S-2	7.29	10.07	1.33	2.07	2.18	10.99	38.88	1.10	18.97	1.69	2.96	-	2.45
S-3	7.80	7.39	-	0.06	4.13	5.59	43.40	5.41	1.64	5.48	7.38	-	11.72
S-4	9.66	12.20	0.33	1.24	18.35	4.75	32.11	2.75	1.81	5.33	9.39	-	2.08
S-5	5.91	22.34	1.18	2.14	8.07	8.58	33.38	0.80	7.35	3.04	0.35	5.57	1.29

4. Conclusions

(1) Based on the manufacturing process of traditional solution-aging treated (SAT) valves, the

plastic deformation technique of cold upsetting was introduced to obtain the solution-cold upsetting-aging treated (SCUAT) valves. For an exhaust valve made of Ni30 valve steel, the grain size of the SCUAT valve conical surface changed from equiaxed crystal to flat grain, and the overall hardness was increased by 60 $HV_{0.2}$, compared with the SAT valve.

(2) The wear loss of valves was affected by test temperature, and the wear protective oxide film was more easily formed at high temperatures. Under the test temperature of 750 ℃, the wear loss of the SCUAT valve was much less than that at 650 ℃ after the same impact cycles.

(3) Under the same test condition, the wear width and wear area of the SCUAT valve was smaller than that of the SAT valve, the valve wear loss decreased by 34.75% at most, and the total wear loss of the valve-seat insert contact pair decreased by 26.76% at most. The SCUAT valve showed better wear resistance at high temperatures.

(4) Cold upsetting treatment is an effective surface strengthening process to improve the high-temperature wear resistance of the VSF. Cold upsetting treatment on the VSF could be regarded as a potential manufacturing method to produce engine valves with good wear resistance.

Acknowledgments

The authors sincerely thank the financial supports from the National Natural Science Foundation of China (Grant No.52205185 and No.12272094). In addition, the authors would like to express the sincere acknowledgment to former Chairman Tao Zhang from Huaiji Dengyun Auto–parts (Holding) Co., LTD. The valuable guidance and advice from Senior Engineer Huahuan Luo and Engineer Deci Kong from Huaiji Dengyue Valve Co., Ltd. are also highly appreciated.

References

[1] L.A.B. Mascarenhas, J.D.O. Gomes, C. Barbosa, et al., Analysis of the tribological behaviour of an automotive engine exhaust valve and a valve seat using a newly developed high temperature workbench, Journal of the Brazilian Society of Mechanical Sciences and Engineering 37 (6) (2015) 1743-1749, https://doi.org /10.1007 /s40430-015-0419-0.

[2] F. Lai, S. Qu, Y. Duan, et al., The wear and fatigue behaviours of hollow head & sodium filled engine valve, Tribology International 128 (2018) 75-88, https://doi.org/10.1016/j.triboint.2018.07.015.

[3] Y.S. Wang, Introduction to engine valvetrains, Warrendale: SAE International, 2007.

[4] J.S. Sidhu, G.S. Lathkar, S.B. Sharma, Design of epoxy based resin composites for automotive applications: a case study on IC engine valve guide, Journal of The Institution of Engineers (India): Series C 100 (2019) 283-288, https://doi.org/10.1007/s40032-017-0439-x.

[5] R. Lewis, R.S. Dwyer-Joyce, Automotive engine valve recession, London: Engineering Research Series, 2002.

[6] P. Forsberg , D. Debord, S. Jacobson, Quantification of combustion valve sealing interface sliding—A novel experimental technique and simulations, Tribology International 69 (2014) 150-155. https://doi.org/10.1016/ j.triboint.2013.09.014.

[7] J.K. Chun, S.J. Hong, A study on engine valve and seat insert wearing depending on speed change, Transaction of the Korean Society of Automotive Engineers 11 (6) (2003) 14-20, https://doi.org/10.4271/2004-01-1655.

[8] F. Lai, S. Qu, H. Qin, et al., A comparison of wear behaviour of heat-resistant steel engine valves and TiAl engine valves, Proceedings of the Institution of Mechanical Engineers, Part J: Journal of Engineering Tribology 234 (10) (2020) 1549-1562, https://doi.org/10.1177/1350650119872093.

[9] F. Bayata, A.T. Alpas, The high temperature wear mechanisms of iron-nickel steel (NCF 3015) and nickel based superalloy (inconel 751) engine valves, Wear 480 (2021) 203943. https://doi.org/10.1016/ j.wear.2021.203943.

[10] F. Lai, S. Qu, R. Lewis, et al., The influence of ultrasonic surface rolling on the fatigue and wear properties of 23-8N engine valve steel. International Journal of Fatigue 125 (2019) 299-313, https://doi.org/10.1016/j.ijfatigue. 2019.04.010.

[11] M. Lou, A.T. Alpas, High temperature wear mechanisms in thermally oxidized titanium alloys for engine valve applications, Wear 426 (2019) 443-453, https://doi.org/10.1016/j.wear.2018.12.041.

[12] P.M. Lerman, R.P.F. de Almeida, Heavy duty valves with enhanced performance through nitriding treatment, SAE Technical Paper (2015), https://doi.org/10.4271/2015-36-0240.

[13] Y.H. Wu, H.J. Yang, R.P. Guo, et al., Tribological behavior of boronized Al0.1CoCrFeNi high-entropy alloys under dry and lubricated conditions. Wear 460 (2020) 203452, https://doi.org/10.1016/j.wear.2020.203452.

[14] E.R. Sivakumar, P. Senthilkumar, M. Sreenivasan, et al., Experimental investigation of H-DLC coated exhaust valve characteristics of a diesel engine, Materials Today: Proceedings 33 (2020) 675-681, https://doi.org/10.1016/j.matpr.2020.05.776.

[15] N. Li, Q. Wang,. Niu, et al., Microstructure and wear behaviors of 17-4 PH stainless steel fabricated by laser cladding with post laser shock peening treatment, Wear 538 (2024) 205207, https://doi.org/10.1016/j.wear.2023.205207.

[16] E.P. Shalunov, Y.O. Vladimirova, Heat-and wear-resistant composite material based on copper powder for heavy duty friction pairs, Materials Today: Proceedings 38 (2021) 1784-1788, https://doi.org/10.1016/j.matpr.2020.08.266.

[17] S.C. Ram, K. Chattopadhyay, I. Chakrabarty, High temperature tensile properties of centrifugally cast in-situ Al-Mg2Si functionally graded composites for automotive cylinder block liners, Journal of Alloys and Compounds 724 (2017) 84-97, https://doi.org/10.1016/j.jallcom.2017.06.306.

[18] S.C. Ram, K. Chattopadhyay, I. Chakrabarty, Microstructures and high temperature mechanical properties of A356-Mg2Si functionally graded composites in as-cast and artificially aged (T6) conditions, Journal of Alloys and Compounds 805 (2019) 454-470, https://doi.org/10.1016/j.jallcom.2019.07.075.

[19] S.C. Ram, K. Chattopadhyay, I. Chakrabarty, Dry sliding wear behavior of A356 alloy/Mg 2 sip functionally graded in-situ composites: effect of processing conditions, Tribology in Industry 38(3) 2016 371-384.

[20] S.C. Ram, K. Chattopadhyay, I. Chakrabarty, Effect of magnesium content on the microstructure and dry sliding wear behavior of centrifugally cast functionally graded A356-Mg2Si in situ composites, Materials Research Express 5(4) 2018 046535, https://doi.org/10.1088/2053-1591/aabbea.

[21] W. Sun, N. Wu, X. Shao, et al., The effects of different strengthening treatments on wear performance of ZL109 aluminum alloy at high temperature, Wear 558 (2024) 205592, https://doi.org/10.1016/j.wear.2024.205592.

[22] A. Hatano, K. Namiki, Application of hard shot peening to automotive transmission gears, SAE Technical Paper (1992), https://doi.org/10.4271/920760.

[23] K. Zheng, X. Zhao, L. Pan, et al., Ultrasonic rolling strengthening of TC11 titanium alloy surface: Corrosion and wear properties under extreme conditions, Wear 550 (2024) 205415, https://doi.org/10.1016/j.wear.2024.205415.

[24] G. Sun, F.H. Wang, D.C. Kong, et al., An engine valve strengthening method and engine valve, China patent, ZL 201910875085.0.2019-09-16. [in Chinese]

[25] H. Ji, J. Liu, B. Wang, et al., Numerical analysis and experiment on cross wedge rolling and forging for engine valves, Journal of materials processing technology 221 (2015) 233-242, https://doi.org/10.1016/j.jmatprotec.2015.02.007.

[26] M. Yin, L. Zhang, L. Huang, et al., Effect of ultrasonic surface rolling process on the fretting tribocorrosion behaviors of Inconel 690 alloy, Tribology International 184 (2023) 108451, https://doi.org/10.1016/j.triboint.2023.108451.

[27] Z.M. Liu, Bench test method for enhanced wear of automotive engine valve - valve seat insert, China Planning Press (2006) [in Chinese].

[28] H.L.C. Mainet, L.P. Cabrera, E. Rodriguez, et al., TiN nanoparticles: small size-selected fabrication and their quantum size effect, Nanoscale Research Letters 7 (1) (2012) 80, https://doi.org/10.1186/1556-276X-7-80.

[29] G. Yang, H. Lai, W. Lin, et al., Approaching the structure-property relationship of sintered metal nano/microparticles from the perspective of the agglomerate size effect, Powder Technology 399 (2022) 117254, https://doi.org/10.1016/j.powtec.2022.117254.

[30] S. Jiang, J. Hewett, I.P. Jones, et al., Effect of misorientation angle and chromium concentration on grain boundary sensitisation in an austenitic stainless steel, Materials Characterization 164 (2020) 110343, https://doi.org/10.1016/j.matchar.2020.110343

[31] S.K. Ghosh, Influence of cold deformation on the aging behaviour of Al-Cu-Si-Mg alloy, Journal of Materials Science & Technology 27 (3) (2011) 193-198, https://doi.org/10.1016/S1005-0302（11）60048-0.

[32] M. Kamaya, Correction of step size dependency in local misorientation obtained by EBSD measurements: Introducing equidistant local misorientation, Ultramicroscopy 259 (2024) 113928, https://doi.org/10.1016/j.ultramic.2024.113928.

[33] V. Randle, O. Engler, Introduction to texture analysis: macrotexture, microtexture and orientation mapping, Boca Raton: CRC Press, (2014).

[34] X. Li, J.J. Shi, C.H. Wang, et al. Effect of heat treatment on microstructure evolution of Inconel 718 alloy fabricated by selective laser melting, Journal of Alloys and Compounds 764 (2018) 639-649, https://doi.org/10.1016/ j.jallcom.2018.06.112.

[35] X.Y. Jia, S.G. Qu, X.F. Hu, et al., Study on the tribology properties of iron-nickel-base NCF 3015 steel for engine valve at high temperatures, Journal of Materials Engineering and Performance 32 (4) (2022) 1545-1557,

https://doi.org/10.1007/s11665-022-07246-w.

[36] P. Forsberg, P. Hollman, S. Jacobson, Wear mechanism study of exhaust valve system in modern heavy duty combustion engines, Wear 271 (9-10) (2011) 2477-2484, https://doi.org/10.1016/j.wear.2010.11.039

[37] L.A.B. Mascarenhas, J.D.O. Gomes, V.E. Beal, et al., Design and operation of a high temperature wear test apparatus for automotive valve materials, Wear 342-343 (2015) 129-137, https://doi.org/10.1016/j.wear.2015.08.017.

[38] M.G. Yin , H.Y. Yin, Q.Q. Zhang, et al., Effect of ultrasonic surface rolling process on the high temperature fretting wear behavior of Inconel 690 alloy, Wear 500-501 (2022) 204347, https://doi.org/10.1016/j.wear.2022.204347.

[39] T.F.J. Quinn, Review of oxidational wear: Part I: The origins of oxidational wear, Tribology International 16 (5) (1983) 257-271, https://doi.org/10.1016/0301-679x(80)90031-6.

[40] A. Renz, B. Prakash, J. Hardell, et al., High-temperature sliding wear behaviour of Stellite®12 and Tribaloy®T400, Wear 402-403 (2018) 148-159, https://doi.org/10.1016/j.wear.2018.02.013.

[41] Y. Jian, Z. Huang, J. Xing, et al., Effects of chromium additions on the three-body abrasive wear behavior of Fe-3.0 wt% B alloy, Wear 378 (2017) 165-173, https://doi.org/10.1016/j.wear.2017.02.042